*First*                                             *Last*

ASME Paper Title: Experimental and numerical assessment of local resonance phenomena in 3D-printed acoustic

metamaterials

Authors:          David Roca, Teresa Pamies, Juan Cante, Oriol Lloberas Valls, Javier Oliver

ASME Journal Title:  Journal of vibration and acoustics. Transactions of the ASME

Volume/Issue _____142/2_____ Date of Publication (VOR* Online) _ December 18, 2019

ASME Digital Collection URL: https://asmedigitalcollection.asme.org/vibrationacoustics/article-abstract/doi/10.1115/1.4045774/1072148/Experimental-and-numerical-assessment-o local?redirectedFrom=fulltext

DOI:          10.1115/1.4045774

*VOR (version of record)

# Experimental and numerical assessment of local resonance phenomena in 3D-printed acoustic metamaterials

**D. Roca**[*]
Centre Internacional de Mètodes
Numèrics en Enginyeria (CIMNE)
Universitat Politècnica de Catalunya
Campus Nord UPC, Mòdul C-1 101,
c/ Jordi Girona 1-3,
08034 Barcelona, Spain
Email: droca@cimne.upc.edu

**T. Pàmies**

Laboratori d'Enginyeria
Acústica i Mecànica (LEAM)
Universitat Politècnica de Catalunya
Campus Terrassa UPC, Edifici TR45,
c/ Colom 11,
08222 Terrassa, Spain

**J. Cante**

Centre Internacional de Mètodes
Numèrics en Enginyeria (CIMNE)
Universitat Politècnica de Catalunya
Campus Nord UPC, Mòdul C-1 101,
c/ Jordi Girona 1-3,
08034 Barcelona, Spain

**O. Lloberas-Valls**

Centre Internacional de Mètodes
Numèrics en Enginyeria (CIMNE)
Universitat Politècnica de Catalunya
Campus Nord UPC, Mòdul C-1 101,
c/ Jordi Girona 1-3,
08034 Barcelona, Spain

**J. Oliver**

Centre Internacional de Mètodes
Numèrics en Enginyeria (CIMNE)
Universitat Politècnica de Catalunya
Campus Nord UPC, Mòdul C-1 101,
c/ Jordi Girona 1-3,
08034 Barcelona, Spain

## ABSTRACT

*The so called Locally Resonant Acoustic Metamaterials (LRAM) are a new kind of artificially engineered materials capable of attenuating acoustic waves. As the name suggests, this phenomenon occurs in the vicinity of internal frequencies of the material structure, and can give rise to acoustic bandgaps. One possible way to achieve this is by considering periodic arrangements of a certain topology (unit cell), smaller in size than the characteristic wavelength. In this context, a computational model based on a homogenization framework has been developed from which one can obtain the aforementioned resonance frequencies for a given LRAM unit cell design in the sub-wavelength regime, which is suitable for low-frequency applications. Aiming at validating both the proposed numerical model and the local resonance phenomena responsible for the attenuation capabilities of such materials, a 3D-printed prototype consisting of a plate with a well selected LRAM unit cell design has been built and its*

---

[*]Corresponding author

*acoustic response to normal incident waves in the range between 500 and 2000 Hz has been tested in an impedance tube. The results demonstrate the attenuating capabilities of the proposed design in the targeted frequency range for normal incident sound pressure waves and also establish the proposed formulation as the fundamental base for the computational design of 3D-printed LRAM-based structures.*

## 1 Introduction

The notion of metamaterials as artificially engineered structures capable of exhibiting properties which cannot be found in ordinary materials has awoken the interest among both the scientific and industrial communities due to their potential applications [1]. Even though the concept was born in the context of electromagnetism, where materials behave as if they had negative refractive indices, the idea rapidly extended to other fields where wave propagation phenomena occur. Specifically for this matter, in the context of acoustics, metamaterials show the ability to effectively stop waves from propagating in certain frequency ranges, typically called frequency bandgaps, due to local resonance effects [2]. These kinds of phenomena are triggered when the material is excited by an acoustic wave at a frequency close to certain internal resonance frequencies, typically related to the metamaterial's topology in the lower scale, effectively causing significant levels of attenuation of the wave's amplitude from a macroscopic point of view [3,4]. This is interesting in applications where significant levels of acoustic attenuation need to be achieved for specific frequency regions, especially in the low-frequency range (i.e. around 1000 Hz), where more conventional solutions would require impractical amounts of mass.

Among the first actual realizations of acoustic metamaterials, Liu et al. [2] built a composite structure that possessed negative elastic constants, exhibiting bandgaps in localized regions of the frequency spectrum. Research in this line was followed by several other experimental demonstrations [5–8], in which the acoustic metamaterial consisted of a polymer-based matrix structure with embedded silicone rubber-coated metal inclusions. In fact, this is the typical configuration that allows local resonance phenomena to arise, since the relative rigidity of the polymer matrix allows resonance modes to be localized in each cell and the combination of the low stiffness of the silicone rubber with the high density of the metal inclusions trigger these internal resonance modes in the low-frequency range. Other acoustic metamaterial configurations based on the concept of local resonance have also been explored, including the use of binary materials [9], materials with porous topologies or hollow cavities [10,11] or contact-based metamaterials consisting of microspheres attached to a membrane [12,13], among others. Configurations based on resonating beams [14], plates [15,16] or membranes [17] have also been explored. While most studies have been carried out on periodic arrangements, recent works show that irregularities and random structures also exhibit attenuation capabilities and can even improve them with proper selection of certain parameters [18–21].

In terms of numerical modelling of acoustic metamaterials and their related phenomena, several works can be found in the literature. For instance, in Xiao et al. [22] an analytical model for a simple 1D string with spring-mass resonators attached is developed in order to understand the bandgap formation mechanisms. A more sophisticated analysis based on the Bloch-Floquet theory has been performed by Liu and Hussein [23] to study wave propagation effects in periodic media, which has been used, for instance, to study the dispersion properties of 2D and 3D periodic unit cells [24]. Also in this line, Bloch-based models have been used to characterize resonance modes responsible for local resonance effects in periodic structures [25]. In the homogenization field, Fokin et al. [26] proposed a method to retrieve effective properties of LRAM from experimental measurements of the transmission and reflection coefficients, while in Nemat-Nasser et al. [27] a homogenization method based on the Floquet theory for elastic composites with periodic structures is presented. In more recent works, computational homogenization frameworks based on multiscale variational principles have also been proposed and proved to be capable of accounting for local resonance phenomena [28–32].

While the concepts and realizations discussed so far have provided a better understanding of the local resonance phenomenon, and served as a proof of the properties of acoustic metamaterials, they are still far from actual industrial application, mainly due to limitations in the construction process. In this regard, a new kind of acoustic metamaterial has been devised, which is meant to be built entirely through emerging additive manufacturing techniques (i.e. 3D-printing). Experiments have been performed focused on the vibration attenuation properties of 3D-printed structures such as in McGee et al. [33], where both experimental and numerical analysis of a 3D-printed foam based on resonating hollow-spheres and binders have been performed. Given the material properties of common 3D-printing materials available and current limitations of manufacturing techniques, proper experimental evaluation of acoustic attenuation capabilities of these kinds of devices have been more challenging, since either their dimensions or the frequency ranges of operation are unsuitable for common measuring devices such as impedance tubes. However, some attempts have been made and can be found in the literature. As examples, Claeys et al. [34] have carried out experimental tests measuring the insertion loss of acoustic enclosures consisting of unit cells with internal resonators, built entirely through Selective Laser Sintering (SLS) methods. On the other hand, Leblanc and Lavie [35] have measured the transmission loss in a 3D-printed single cell of a membrane-type acoustic metamaterial built with Fused Deposition Modeling (FDM) technology. Following this line, the aim of this work is to present both a numerical and an experimental assessment of the acoustic attenuating capabilities, namely the normal-incidence transmission loss, to demonstrate the appearance of local resonance effects in a metamaterial entirely 3D-printed through Multi Jet Fusion (MJF) technique. To this end, a computational model has been used to obtain the relevant resonant modes and frequencies for a

LRAM unit cell design, and the corresponding 3D-printed samples in the shape of panels have been built in order to test their transmission loss capabilities at normal incidence.

## 2 Experimental set-up

The impedance tube method has been typically used to evaluate the acoustic performance of materials. It consists of two impedance tubes of constant section, with a speaker on one end and an anechoic termination on the other. The material sample to be tested is placed between both tubes and the sound pressure level of the acoustic wave emitted by the speaker is measured at different locations along the tube with microphones. In particular, the reflection coefficient can be obtained through measurements from two or more microphones located at different distances from the sample's incident surface in the front tube section. For transmission loss determination, typically two additional microphones are placed on the rear tube section.

While in the standard method for measuring the normal incidence sound transmission loss, a sample of the material is put inside the tubes (and so it needs to be cut so that it fills the whole section of the enclosure), a slightly modified version was proposed by Ho et al. [6], which is suitable for locally resonant acoustic metamaterials testing. In this case, a sample panel is pressed and held firmly between both impedance tubes. This method allows more flexibility for the samples shape and configuration while also being able to capture the local resonance behaviour expected, as reported in Ho et al. [6].

The apparatus employed for measuring the normal incidence sound transmission loss consists of two impedance tubes with a 8 cm × 8 cm section with 4 cm thick medium-density fibreboard (MDF) walls for isolating the acoustic wave inside from environmental sources. A 3.3 inch loudspeaker (4 Ohm, 30 Watts) connected to an amplifier is located on one end of the front tube, and the last 30 cm of the other tube are filled with a polyurethane foam, acting as absorbing material in order to guarantee an anechoic termination. A total of 4 1/2" prepolarized microphones with an ICP preamplifier are placed at different positions: two on the front tube positioned at 10 and 17.6 cm from the sample's front surface, and two on the rear tube positioned also at 10 and 17.6 cm from the sample's rear surface. According to ASTM E1050-98 [36], the section size and separation between each pair of microphones should guarantee valid results in the frequency range between 200 and 2000 Hz. A schematic representation of the experimental setup can be found in Figure 1.

The transmission of each sample panel can be obtained from the measurements of the four microphones. Considering the acoustic wave inside the tube is plane, it can be expressed, in the frequency domain, as

$$P_f(x,\omega) = A(\omega)e^{i\kappa x} + B(\omega)e^{-i\kappa x} \tag{1}$$

in the front tube, and

$$P_r(x,\omega) = C(\omega)e^{i\kappa x} + D(\omega)e^{-i\kappa x} \tag{2}$$

in the rear tube.

In the above equations, $x$ refers to the distance with respect to the front surface of the sample panel, $\omega$ is the wave's frequency, $\kappa = \omega/c$ is the wavenumber (with $c$ being the speed of sound in air) and $A$, $B$, $C$ and $D$ are the complex amplitudes of (a) the wave emitted by the loudspeaker, (b) the wave reflected by the panel in the front tube, (c) the wave transmitted through the panel to the rear tube and (d) the wave reflected on the rear tube, respectively.

Under anechoic termination condition in the rear tube, i.e. $D = 0$, the transmission $T$ of the sample panel can be obtained directly as

$$T(\omega) = \frac{C(\omega)}{A(\omega)}. \tag{3}$$

The coefficients $A$ and $C$ appearing in equation (3) can be obtained from equations (1) and (2) by replacing $P_f$ and $P_r$ with the corresponding sound pressure values measured at each frequency:

$$P_1(\omega) = A(\omega)e^{i\kappa x_1} + B(\omega)e^{-i\kappa x_1}; \quad \text{with } x_1 = -17.6 \text{ cm}, \tag{4}$$

$$P_2(\omega) = A(\omega)e^{i\kappa x_2} + B(\omega)e^{-i\kappa x_2}; \quad \text{with } x_2 = -10 \text{ cm}, \tag{5}$$

$$P_3(\omega) = C(\omega)e^{i\kappa x_3} + D(\omega)e^{-i\kappa x_3}; \quad \text{with } x_3 = d + 10 \text{ cm}, \tag{6}$$

$$P_4(\omega) = C(\omega)e^{i\kappa x_4} + D(\omega)e^{-i\kappa x_4}; \quad \text{with } x_2 = d + 17.6 \text{ cm}, \tag{7}$$

where $d$ is the thickness of the sample panel. The values of each $P_k$ (the subscript $k$ here refers to each microphone, i.e. $k = 1, 2, 3$ or $4$) have been obtained from the Fourier transform of the time samples of actual pressure measurements in the corresponding microphone positions. For this experiment, a pink noise (a noise source on the whole audible frequency range with equal amount of energy for each octave) has been emitted by the loudspeaker and pressure measurements at each position have been recorded for a total of 10 seconds, with a sample time of $2 \times 10^{-4}$ seconds.

The procedure described in ASTM E1050-98 [36] has been considered for correcting the amplitude and phase of the measured pressure values. To do so, a calibration transfer function, $H_k^c$ has been computed for each microphone:

$$H_k^c(\omega) = \sqrt{\frac{P_1^I(\omega)}{P_k^I(\omega)} \frac{P_k^{II}(\omega)}{P_1^{II}(\omega)}}, \tag{8}$$

where $P_1^I$ and $P_k^I$ are the complex Fourier transformed pressures measured by microphones 1 and $k$ for the empty tube case (without a sample panel), and $P_1^{II}$ and $P_k^{II}$ are the corresponding values for the same case but in which the microphones 1 and $k$ have switched positions. Note that the microphone position 1 is being used as a reference.

Now, from equations (4) and (5) and by correcting the pressure values at each microphone position with their corresponding calibration transfer function, it can be obtained

$$A(\omega) = i \frac{P_1 H_1^c e^{-i\kappa x_2} - P_2 H_2^c e^{-i\kappa x_1}}{2 \sin(x_2 - x_1)}, \tag{9}$$

while from equations (6) and (7),

$$C(\omega) = i \frac{P_3 H_3^c e^{-i\kappa x_4} - P_4 H_4^c e^{-i\kappa x_3}}{2 \sin(x_4 - x_3)}. \tag{10}$$

Finally, by inserting into equation (3) the values obtained for coefficients $A$ and $C$ from equations (9) and (10), respectively, the transmission loss can be obtained as

$$\mathrm{TL}(\omega) = 10 \log_{10} \left( \frac{1}{|T|^2} \right). \tag{11}$$

It should be noted that the anechoic termination condition has been validated in the employed apparatus by comparing the transmission loss for an empty tube case (no panel) obtained with equation (3) with that obtained considering all four coefficients,

$$T(\omega) = \frac{A(\omega) \cdot C(\omega) - B(\omega) \cdot D(\omega)}{A^2(\omega) - D^2(\omega)}, \tag{12}$$

and verifying that they give almost the same result with differences of less than 0.2 dB.

## 3 Numerical model

The computational homogenization framework introduced by Roca et al. [31] will be used in this work to characterize the modes and frequencies responsible for local resonance phenomena to arise and to identify the metamaterial unit cell homogenized properties to understand the response of the medium in the impedance tube. Even though a detailed description of the model can be found in Roca et al. [31, 32], a brief summary will also be presented here, for completeness.

The model is based on multiscale theory and can be applied as long as the unit cell size, $\ell_\mu$, is much smaller (at least an order of magnitude) than the macroscopic wavelength, $\lambda$, i.e.

$$\lambda \gg \ell_\mu. \tag{13}$$

The whole formulation is grounded on the application of the linear and angular momentum balance postulates for Continuum Mechanics in the macroscale, which read, respectively,

$$\nabla_{\mathbf{x}} \cdot \boldsymbol{\sigma}(\mathbf{x},t) = \dot{\mathbf{p}}(\mathbf{x},t), \tag{14}$$

$$\boldsymbol{\sigma}(\mathbf{x},t) = \boldsymbol{\sigma}^{\mathrm{T}}(\mathbf{x},t), \tag{15}$$

where $t$ refers to time, $\mathbf{x}$ are the spatial coordinates in the macroscale, $\boldsymbol{\sigma}$ is the macroscopic effective second-order stress tensor and $\dot{\mathbf{p}}$ is the macroscopic effective inertial force density. Note that the symbol $(\bullet)^{\mathrm{T}}$ is used to denote the transpose of $(\bullet)$. To each point $\mathbf{x}$ in the macroscale, a representative volume element (RVE) or, in this case, a unit cell, is assigned, and a kinematic relation for the displacement field is imposed, in particular,

$$\mathbf{u}_{\mu}(\mathbf{y},t) = \mathbf{u}(\mathbf{x},t) + (\mathbf{y} - \mathbf{y}^{(0)}) \cdot \nabla_{\mathbf{x}} \mathbf{u}(\mathbf{x},t) + \tilde{\mathbf{u}}_{\mu}(\mathbf{y},t) \tag{16}$$

where the subscript $\mu$ is used to distinguish microscale variables from their macroscopic counterparts, $\mathbf{y}$ are the spatial coordinates in the microscale context, $\mathbf{y}^{(0)}$ are the coordinates of the centroid of the RVE and $\tilde{\mathbf{u}}_{\mu}$ is a microfluctuation field, satisfying the minimal kinematic conditions

$$\langle \tilde{\mathbf{u}}_{\mu} \rangle_{\Omega_{\mu}} = \mathbf{0}, \tag{17}$$

$$\langle \nabla_{\mathbf{y}}^{\mathrm{S}} \tilde{\mathbf{u}}_{\mu} \rangle_{\Omega_{\mu}} = \mathbf{0}. \tag{18}$$

Note that the notation $\langle \bullet \rangle_{\Omega_{\mu}}$ is used to refer to the mean value of $(\bullet)$ integrated over the RVE volume $\Omega_{\mu}$, i.e.

$$\langle \bullet \rangle_{\Omega_{\mu}} = \frac{1}{|\Omega_{\mu}|} \int_{\Omega_{\mu}} (\bullet) d\Omega. \tag{19}$$

Finally, an energetic equivalence between both scales is established, by means of the generalized Hill-Mandel principle, which reads

$$\dot{\mathbf{p}} \cdot \dot{\mathbf{u}} + \boldsymbol{\sigma} : \nabla_{\mathbf{x}}^{\mathrm{S}} \dot{\mathbf{u}} = \langle \dot{\mathbf{p}}_{\mu} \cdot \dot{\mathbf{u}}_{\mu} + \boldsymbol{\sigma}_{\mu} : \nabla_{\mathbf{y}}^{\mathrm{S}} \dot{\mathbf{u}}_{\mu} \rangle_{\Omega_{\mu}}, \ \forall \dot{\mathbf{u}}, \nabla_{\mathbf{x}}^{\mathrm{S}} \dot{\mathbf{u}}, \tag{20}$$
$$\forall \dot{\mathbf{u}}_{\mu} \in \mathcal{U}_{\mu},$$

where $\mathcal{U}_{\mu}$ is the space of admissible microdisplacement fields, i.e. those satisfying equation (16) along with conditions (17) and (18), and the superscript $(\bullet)^{\mathrm{S}}$ is used to indicate the symmetric component of tensor $(\bullet)$. From the variational statement given by equation (20), and after considering the kinematic restrictions of equations (16) to (18), one can obtain the following relations (again, the reader is referred to Roca et al. [31] for details):

$$\boldsymbol{\sigma} = \langle \boldsymbol{\sigma}_{\mu} + (\mathbf{y} - \mathbf{y}^{(0)}) \otimes^{\mathrm{S}} \dot{\mathbf{p}}_{\mu} \rangle_{\Omega_{\mu}}, \tag{21}$$

$$\dot{\mathbf{p}} = \langle \dot{\mathbf{p}}_{\mu} \rangle_{\Omega_{\mu}}, \tag{22}$$

where the symbol $\otimes^{\mathrm{S}}$ refers to the symmetric outer product, i.e. $\mathbf{a} \otimes^{\mathrm{S}} \mathbf{b} = (\mathbf{a} \otimes \mathbf{b} + \mathbf{b} \otimes \mathbf{a})/2$. Then, the weak form of the RVE problem, upon the introduction of the test function $\delta \mathbf{u}_{\mu} \equiv \check{\mathbf{u}}_{\mu}$, reads

$$\langle \dot{\mathbf{p}}_{\mu} \cdot \delta \mathbf{u}_{\mu} + \boldsymbol{\sigma}_{\mu} : \nabla_{\mathbf{y}}^{\mathrm{S}} \delta \mathbf{u}_{\mu} \rangle_{\Omega_{\mu}} = 0, \ \forall \mathbf{u}_{\mu} \in \mathcal{U}_{\mu}, \tag{23}$$
$$\forall \delta \mathbf{u}_{\mu} \in \mathcal{U}_{\mu}^{0},$$

where $\mathcal{U}_\mu^0$ is the space of admissible microfluctuation fields (i.e. satisfying equations (17) and (18)). Then, by considering

$$\boldsymbol{\sigma}_\mu = \mathbf{C}_\mu : \nabla_{\mathbf{y}}^{\mathrm{S}} \mathbf{u}_\mu + \boldsymbol{\eta}_\mu : \nabla_{\mathbf{y}}^{\mathrm{S}} \dot{\mathbf{u}}_\mu, \tag{24}$$

$$\dot{\mathbf{p}}_\mu = \rho_\mu \ddot{\mathbf{u}}_\mu, \tag{25}$$

where $\mathbf{C}_\mu$ is the fourth-order constitutive tensor, $\boldsymbol{\eta}_\mu$ is a viscosity fourth-order tensor accounting for viscoelastic effects and $\rho_\mu$ is the mass density distribution of the RVE, the variational statement given by equation (23) can be used to find the microfluctuation field solution, $\tilde{\mathbf{u}}_\mu$, in terms of the macroscopic displacement and displacement gradient, $\mathbf{u}, \nabla_{\mathbf{x}}\mathbf{u}$, which become *actions* in the resulting system.

The resolution scheme that follows is based on two main simplifying hypotheses:

(a) The separation of scales condition given by equation (13) is satisfied so that the natural frequencies triggering local resonance effects arising in the low-frequency region, far below the range where the first RVE deformation modes appear.

(b) The centre of mass of the RVE is close enough to its centroid so that the inertial contributions on the effective macroscopic stress can be neglected.

The first hypothesis (a) allows us to neglect the inertial response due to macroscopic deformation actions, because they will not be relevant in the frequency range of interest. This makes it possible to split the system into a quasi-static component whose action is simply the macroscopic strain, $\nabla_{\mathbf{x}}^{\mathrm{S}}\mathbf{u}$, and an inertial component whose action becomes the macroscopic acceleration, $\ddot{\mathbf{u}}$. From the quasi-static subsystem, an expression for the macroscopic stress tensor can be obtained, relating it to the macroscopic strain through an effective constitutive tensor:

$$\boldsymbol{\sigma} = \mathbf{C}^{\mathrm{eff}} : \nabla_{\mathbf{x}}^{\mathrm{S}} \mathbf{u} + \boldsymbol{\eta}^{\mathrm{eff}} : \nabla_{\mathbf{x}}^{\mathrm{S}} \dot{\mathbf{u}}. \tag{26}$$

The terms $\mathbf{C}^{\mathrm{eff}}$ and $\boldsymbol{\eta}^{\mathrm{eff}}$ in the previous equation are obtained applying the classical homogenization theory to the quasi-static system, i.e. by imposing periodic boundary conditions on the RVE system under the action of a macroscopic strain. By performing a Galerkin-based Finite Element (FE) discretization, the system can be solved yielding

$$\mathbf{C}^{\mathrm{eff}} = \widetilde{\mathbb{Y}}^{\mathrm{T}} \mathbb{K}_\mu \widetilde{\mathbb{Y}}, \tag{27}$$

$$\boldsymbol{\eta}^{\mathrm{eff}} = \widetilde{\mathbb{Y}}^{\mathrm{T}} \mathbb{C}_\mu \widetilde{\mathbb{Y}}, \tag{28}$$

with

$$\widetilde{\mathbb{Y}} = \mathbb{Y} - \mathbb{P}(\mathbb{P}^{\mathrm{T}} \mathbb{K}_\mu \mathbb{P})^{-1} \mathbb{P}^{\mathrm{T}} \mathbb{K}_\mu \mathbb{Y}, \tag{29}$$

where $\mathbb{K}_\mu$ is the RVE stiffness matrix, $\mathbb{C}_\mu$ is the RVE damping matrix, $\mathbb{P}$ is a boolean matrix imposing the periodic boundary conditions and $\mathbb{Y}$ is a matrix containing the nodal coordinates, $\hat{\mathbf{y}}^{(i)}$, arranged such that

$$\mathbb{Y} = \begin{bmatrix} & & & \vdots & & \\ \hat{y}_1^{(i)} & 0 & 0 & 0 & \hat{y}_3^{(i)}/2 & \hat{y}_2^{(i)}/2 \\ 0 & \hat{y}_2^{(i)} & 0 & \hat{y}_3^{(i)}/2 & 0 & \hat{y}_1^{(i)}/2 \\ 0 & 0 & \hat{y}_3^{(i)} & \hat{y}_2^{(i)}/2 & \hat{y}_1^{(i)}/2 & 0 \\ & & & \vdots & & \end{bmatrix}. \tag{30}$$

The second hypothesis (b) allows us to condense all the inertial effects into a macroscopic inertial force density term, including all the local resonance phenomena that are the focus of this analysis. In particular, by combining equations (22) and (16) (considering, by the definition of $\mathbf{y}^{(0)}$ as the centroid of the RVE, $\langle \mathbf{y} - \mathbf{y}^{(0)} \rangle_{\Omega_\mu} = \mathbf{0}$), one can obtain

$$\dot{\mathbf{p}} = \bar{\rho} \ddot{\mathbf{u}} + \langle \rho_\mu \ddot{\mathbf{u}}_\mu \rangle_{\Omega_\mu}, \tag{31}$$

where $\bar{\rho} = \langle \rho_\mu \rangle_{\Omega_\mu}$ is the volume averaged RVE density and $\langle \rho_\mu \ddot{\mathbf{u}}_\mu \rangle_{\Omega_\mu}$ is the averaged micro-inertial fluctuation contribution and the term responsible for local resonance phenomena. It should be noted that, according to hypothesis (a), the microfluctuation field responsible for those effects is obtained from the inertial subsystem, i.e. the RVE system under the action of a uniform acceleration field and a set of boundary conditions capable of triggering internal resonance modes. This can be achieved, for instance, by prescribing all boundary degrees of freedom, and then solving the modal problem

$$(\mathbb{K}_\mu^* - \lambda_\mu^{*(k)} \mathbb{M}_\mu^*) \hat{\boldsymbol{\phi}}_\mu^{*(k)} = \mathbf{0}. \tag{32}$$

where $\mathbb{K}_\mu$ and $\mathbb{M}_\mu$ are the RVE stiffness and mass matrices, respectively (the superscript $(\bullet)^*$ indicates that the considered boundary conditions have already been applied), $\hat{\boldsymbol{\phi}}_\mu^{*(k)}$ are the resulting mass-normalized eigenvectors and $\lambda_\mu^{*(k)} = (\omega_\mu^{*(k)})^2$ are the eigenvalues. The resulting microfluctuation field can be expressed in terms of internal variables, $q_\mu^{*(k)}$, associated to each of the resonance modes:

$$\tilde{\mathbf{u}}_\mu = \sum_k \mathbb{P}_0 \hat{\boldsymbol{\phi}}_\mu^{*(k)} q_\mu^{*(k)}, \tag{33}$$

where $\mathbb{P}_0$ is a boolean matrix imposing the required boundary conditions. This allows us to express the second term in equation (31) as

$$\langle \rho_\mu \ddot{\mathbf{u}}_\mu \rangle_{\Omega_\mu} = \sum_k \underbrace{\frac{1}{\sqrt{|\Omega_\mu|}} \mathbb{I}^{\mathrm{T}} \mathbb{M}_\mu \mathbb{P}_0 \hat{\boldsymbol{\phi}}_\mu^{*(k)}}_{\mathbf{r}_\mu^{(k)}} \ddot{q}_\mu^{*(k)}, \tag{34}$$

where $\mathbb{I}$ is a column vector of identity second-order tensors. The internal variables are solved through the following microscale system:

$$\ddot{q}_\mu^{*(k)} + \sum_j \omega_\mu^{\mathrm{D}(k,j)} \dot{q}_\mu^{*(j)} + (\omega_\mu^{*(k)})^2 q_\mu^{*(k)} = -\mathbf{r}_\mu^{(k)} \cdot \ddot{\mathbf{u}}, \tag{35}$$

with

$$\omega_\mu^{\mathrm{D}(k,j)} = \frac{1}{|\Omega_\mu|} \boldsymbol{\phi}_\mu^{*(k)\mathrm{T}} \mathbb{P}_0^{\mathrm{T}} \mathbb{C}_\mu \mathbb{P}_0 \boldsymbol{\phi}_\mu^{*(j)}. \tag{36}$$

It is important to note that not all the internal modes obtained from equation (32) are responsible for triggering local resonance effects. In particular, only those with a relevant effect on the macroscale are capable of affecting the metamaterial behaviour, giving rise to frequency bandgaps of acoustic wave attenuation. This discrimination can be easily performed in the present context by evaluating the norm of $\mathbf{r}_\mu^{(k)}$, so

$$||\mathbf{r}_\mu^{(k)}|| \quad \begin{cases} > 0 \rightarrow \text{ the } k\text{-th mode is relevant} \\ = 0 \rightarrow \text{ the } k\text{-th mode is non-relevant} \end{cases} , \tag{37}$$

allowing us to identify the resonance modes and frequencies that trigger local resonance effects for a given RVE design.

## 4 Prototypes design

The sample used for the experimental tests consists of a 120 mm × 120 mm panel 5 mm thick with a 6 × 6 grid of unit cells at the central part, occupying the whole 80 mm × 80 mm tube section. The overall size of each unit cell, 12 mm × 12 mm × 5 mm, is chosen so as to be thin enough for practical applications and to satisfy the separation of scales condition given in equation (13) (note that in the limit case, i.e. for a frequency of 2000 Hz, and considering air as acoustic propagation medium, $\lambda/\ell_\mu > 10$, which is acceptable for triggering local resonance effects and considering the homogenization framework valid).

In Figure 2 a schematic representation of the panel can be found. The metamaterial panel has been monolithically 3D-printed and two $120 \times 120 \times 2$ mm skin panels of the same material have been stuck to each side, in order to isolate and constrain the unit cells, enabling the appearance of internal resonance modes. The unit cells have been designed so that they can be easily 3D-printed from a single block or material, while still being composed of the required elements for local resonance phenomena to arise. Namely, (1) the support rods at the vertices, which become the union points of the cells with the skin panels, isolate each cell, enabling the appearance of internal modes, (2) the central inclusion acts as a mass, becoming the resonating component and (3) the thin attachments allow the unit cell to have relevant resonance modes in the desired frequency range. The panels have been manufactured using Polyamide 11 (PA 11) as 3D-printing material through MJF technology. MJF employs a process similar to SLS in which parts are built by fusing layers of powder polymer. Unlike with SLS, a fusing agent is previously dispensed in the powder in order to promote the absorption of infrared light in each cross section, which typically yields faster and slightly more accurate results, for smaller features, than those obtained with SLS [37].

The homogenization procedure described in Section 3 has been applied to the metamaterial unit cell design with the material properties, provided by the manufacturer, given in Table 1. To do so, a FE mesh of tetrahedra has been used, consisting of around 137000 elements with 3 Gaussian integration points each. In the range between 500 and 2000 Hz, there is only one relevant internal resonance mode (see Figure 3) at a frequency around 1050 Hz, which can trigger local resonance phenomena at the macroscale. It should be noted that the specific design of the unit cell results from the challenge of achieving the internal resonance in the desired frequency range, for the given material properties, while keeping the overall unit cell thin and small (within manufacturability limitations) for practical applications. To do so, (1) the bending stiffness for the thin attachments (which is responsible for the internal resonance mode depicted in Figure 3) must be small and (2) the mass of the resonating inclusion must be large enough. Since the diameters of the attachments are close to the manufacturability limitations, the easiest way to minimize its stiffness to bending is by increasing its length. On the other hand, the mass of the resonating inclusion can be also increased if its volume occupies as much space available in the unit cell as possible. The combination of both yields the flower-like look of the design and enables the appearance of the internal resonance mode at a frequency around 1000 Hz.

## 5 Results
### 5.1 Experimental test

The sample metamaterial panel has been tested and the normal incidence sound transmission loss for a range of frequencies from 500 to 1500 Hz has been obtained as described in Section 2. The results are given in Figure 5 where a region of increased acoustic attenuation can be identified around the frequency of 1000 Hz, very close to the frequency of 1050 Hz, where local resonance phenomena were expected to arise according to the unit cell analysis. For comparison, the same test has been performed on two 120 mm $\times$ 120 mm homogeneous panels 3D-printed with the same material: one with the same equivalent mass as the metamaterial panel assembly, and another with the same thickness, which correspond to panel sizes of 6 and 9 mm, respectively. Figure 5 shows the average results from three different measures for each sample panel. The standard deviation has been measured in each case with values ranging from 0.4 dB for the homogeneous panels to 2.9 dB for the metamaterial case, with this being higher due to very small variations in the peaks location ($< 1\%$) causing larger differences in their transmission loss levels. However, these values are acceptable for a proper qualitative assessment of the phenomenon.

It should be noted that, for the metamaterial panel, aside from the attenuation peak around the frequency of 1000 Hz, there are also two inverted peaks, i.e. transmission peaks, at frequencies of 550 Hz and 1250 Hz. The latter (transmission peak at 1250 Hz) corresponds to the unit cell resonance frequency that typically marks the end of the bandgap region, while the former (transmission peak at 550 Hz) is caused by the pressing of the panel against the sealing component (which allows certain elasticity) that holds it between the two parts of the impedance tube. This inverted peak also appears for the homogeneous panels at the approximate frequencies of 800 and 950 Hz. It should be noted that these results, and in particular the aforementioned transmission peaks, are not expected in standard impedance tube measurements where the sample is placed inside the tube. However, several tests have been performed with different samples (varying materials and geometric properties) in order to verify the repeatability of the results is guaranteed even with the non-standard mounting procedure. It has been observed that even though those peaks are caused by the mounting of the sample, they are related to material and geometric properties of the samples (results are the same for different samples with equivalent material and geometric properties).

### 5.2 Numerical analysis

A macroscopic analysis of the panel response in the tube has been performed, with the simulation setup depicted in Figure 4. The solid domain has been discretized with $18 \times 18 \times 9$ hexahedral elements with 4 Gaussian quadrature points each, and consists of two material phases. The skins and the metamaterial panel outer frame have both been modelled as

standard solid isotropic materials, with the properties given in Table 1. The internal volume, corresponding to where the actual metamaterial unit cells can be found in the panel, has been modelled as a homogenized material with an effective constitutive tensor, $\mathbf{C}^{\text{eff}}$, an effective viscosity tensor $\boldsymbol{\eta}^{\text{eff}}$, an average density, $\bar{\rho}$, and the relevant internal resonance modes and frequencies, $\mathbf{r}_\mu^{(k)}$ and $\omega_\mu^{*(k)}$, along with $\omega_\mu^{\text{D}(k,j)}$, obtained from the unit cell analysis. The procedure described in Roca et al. [32] has been considered in this case for computing the transmission coefficient, from which the transmission loss can be directly obtained. To do so, an appropriate set of displacements and traction forces have been imposed in the sections of the front and rear faces that are exposed to the plane waves travelling inside the tube: (a) an incident wave of arbitrary amplitude towards the panel's front face, (b) a reflected wave, with a reflection coefficient $R$, travelling in the opposite direction, also from the panel's front face, and (c) a transmitted wave, with a transmission coefficient $T$, travelling away from the panel's rear face. In particular, defining $\kappa = \omega/c$ as the wavenumber (with $c$ being the speed of sound in air) and $\rho_a$ as the density of air, the boundary conditions (on both displacements $\mathbf{u}$ and traction forces $\mathbf{f}$) to simulate the normal incident plane wave on the front and rear faces can be written as:

In the front face:

$$\mathbf{n} \cdot \mathbf{u} = (e^{i\kappa x} - Re^{-i\kappa x})e^{-i\omega t}, \tag{38}$$

$$\mathbf{f} = -i\mathbf{n}\rho_a c\omega(e^{i\kappa x} + Re^{-i\omega t})e^{-i\omega t}. \tag{39}$$

In the rear face:

$$\mathbf{n} \cdot \mathbf{u} = Te^{i(\kappa x - \omega t)}, \tag{40}$$

$$\mathbf{f} = -i\mathbf{n}\rho_a c\omega Te^{i(\kappa x - \omega t)}. \tag{41}$$

where $R$ and $T$ become the unknowns. The system from which both coefficients can be obtained has been solved in the frequency domain for a range of 500 frequencies between 500 and 1500 Hz. The results can be seen on Figure 5, where the simulated curves can be compared to the ones obtained from the experimental test with the impedance tube. As for the accuracy of the numerical results, it should be noted that it depends mainly on (a) the number of internal modes considered and (b) the frequency range of study, so that the model is more accurate the smaller the frequency. In particular for this case (normal-incidence plane wave excitation), the next relevant modes frequencies are above 10 kHz, so the single mode considered is enough to guarantee accurate results. More specifically, from previous studies [31], it could be verified that the expected relative error when comparing results to full direct numerical simulations is smaller than 0.1% when the separation of scales is $\lambda/\ell_\mu > 10$ (as in this case), reaching localized peaks of errors around 1% near the resonance frequencies, with these numbers not being largely affected by mesh size.

Note that in order to simulate the effect of the panel's holding against the sealing component (i.e. the transmission peak at 550 Hz), springs of a given stiffness $k = 4000$ N/m have been considered in the pressed area of both the front and rear faces of the panel (see Figure 4). Furthermore, in order to smooth the simulated resonance peaks, an additional analysis has been performed where damping effects have been considered by introducing a certain degree of viscoelastic behaviour to the material (with a viscosity of $\mu = 3000$ Pa·s, chosen in order to fit the experimental results).

## 6 Discussion

Results from Figure 5 show that the metamaterial panel attenuation performance as a response to normal incident acoustic waves around the region where local resonance effects were expected is improved when compared to those of homogeneous panels with the same effective mass or thickness. Even without considering the transmission peaks in the homogeneous panels cases, an increase of 15 to 25 dB from the baseline values can be observed in a frequency range of around 300 Hz. It is worth noting the normal incidence sound transmission loss decrease in the metamaterial panel for frequencies above the upper bandgap limit, which make it a suitable choice especially for low-frequency applications.

On the other hand, from the obtained results in Figure 5, it can be seen that both the experimental and simulated curves' shapes are the same, capturing in each case the attenuation rise around the frequency responsible for the local resonance effects and then the transmission peak indicating the bandgap end. However, it should be noted that there are some differences in the frequencies where the peaks are produced, which are most likely caused by geometrical tolerances in the fabrication process of the samples. In particular, the internal resonance frequency is very sensitive to the thickness of the attachments, causing variations of the order of $\pm 200$ Hz for diameter deviations of $\pm 0.1$ mm. This is an indication that small variations in the geometry of the unit cells can give rise to several attenuation peaks, a fact that, if properly considered in the design process, may be of interest, for instance, when trying to enlarge the effective attenuation band. This shows

the importance of the design process of acoustic metamaterials and how there is room for improvement and optimization towards achieving the desired properties and behaviour. In this regard, the need for very accurate fabrication methods is also of utmost importance in order to achieve the expected results and performance, as unplanned variations of just 12% in the diameter at this scale, can cause a 20% deviation in the expected frequencies. It is important to note that for the present study, measurements have been performed with only one sample panel. However, in order to evaluate the accuracy of the 3D-printed prototype, measurements of the thickness of the attachments have been made, yielding an average value of 0.79±0.03 mm, with a standard deviation of 0.009 mm. This represents around 1.2% variation from the design value (0.8 mm), and while the expected impact on the results should not be large (around 2% deviation in frequency), it certainly is an issue that should be considered when designing unit cell models at this scale with the current state of 3D-printing technologies.

## 7  Conclusions

The results of this work can be used to both confirm the appearance of local resonance effects in 3D-printed acoustic metamaterials as a response to normal incident sound pressure waves, and to validate the proposed numerical scheme as a tool for characterizing such kinds of phenomena. This can be regarded as a first step towards an alternative approach to what has been the standard in acoustic metamaterial unit cell design so far, where instead of achieving the desired metamaterial behaviour by combining two or more materials with different properties, the same effects are obtained with only one material and relying more on geometric and topological aspects of the design. On a next stage, more sophisticated computational techniques, such as topology optimization algorithms, can be involved in the design process in order to achieve optimized designs for targeted sets of properties. Additionally, this novel approach is naturally compatible with emerging manufacturing technologies, which can facilitate the fabrication process, making these materials more appealing and bringing them one step closer to practical applications.

## References

[1] Deymier, P. A., 2013. *Acoustic metamaterials and phononic crystals*, Vol. 173. Springer Science & Business Media.

[2] Liu, Z., Zhang, X., Mao, Y., Zhu, Y., Yang, Z., Chan, C. T., and Sheng, P., 2000. "Locally resonant sonic materials". *Science,* **289**(5485), pp. 1734–1736.

[3] Hussein, M. I., Leamy, M. J., and Ruzzene, M., 2014. "Dynamics of phononic materials and structures: Historical origins, recent progress, and future outlook". *Applied Mechanics Reviews,* **66**(4), p. 040802.

[4] Cummer, S. A., Christensen, J., and Alu, A., 2016. "Controlling sound with acoustic metamaterials". *Nature Reviews Materials,* **1**, p. 16001.

[5] Sheng, P., Zhang, X., Liu, Z., and Chan, C. T., 2003. "Locally resonant sonic materials". *Physica B: Condensed Matter,* **338**(1-4), pp. 201–205.

[6] Ho, K. M., Yang, Z., Zhang, X., and Sheng, P., 2005. "Measurements of sound transmission through panels of locally resonant materials between impedance tubes". *Applied acoustics,* **66**(7), pp. 751–765.

[7] Calius, E. P., Bremaud, X., Smith, B., and Hall, A., 2009. "Negative mass sound shielding structures: Early results". *physica status solidi (b),* **246**(9), pp. 2089–2097.

[8] Wester, E. C., Brémaud, X., and Smith, B., 2009. "Meta-material sound insulation". *Building Acoustics,* **16**(1), pp. 21–30.

[9] Wang, G., Wen, X., Wen, J., Shao, L., and Liu, Y., 2004. "Two-dimensional locally resonant phononic crystals with binary structures". *Physical review letters,* **93**(15), p. 154302.

[10] Boutin, C., and Becot, F. X., 2015. "Theory and experiments on poro-acoustics with inner resonators". *Wave Motion,* **54**, pp. 76–99.

[11] Sainidou, R., Djafari-Rouhani, B., Pennec, Y., and Vasseur, J., 2006. "Locally resonant phononic crystals made of hollow spheres or cylinders". *Physical Review B,* **73**(2), p. 024302.

[12] Khanolkar, A., Wallen, S., Abi Ghanem, M., Jenks, J., Vogel, N., and Boechler, N., 2015. "A self-assembled metamaterial for lamb waves". *Applied Physics Letters,* **107**(7), p. 071903.

[13] Hiraiwa, M., Ghanem, M. A., Wallen, S. P., Khanolkar, A., Maznev, A. A., and Boechler, N., 2016. "Complex contact-based dynamics of microsphere monolayers revealed by resonant attenuation of surface acoustic waves". *Physical review letters,* **116**(19), p. 198001.

[14] Yu, D., Liu, Y., Zhao, H., Wang, G., and Qiu, J., 2006. "Flexural vibration band gaps in euler-bernoulli beams with locally resonant structures with two degrees of freedom". *Physical Review B,* **73**(6), p. 064301.

[15] Wu, T.-T., Huang, Z.-G., Tsai, T.-C., and Wu, T.-C., 2008. "Evidence of complete band gap and resonances in a plate with periodic stubbed surface". *Applied Physics Letters,* **93**(11), p. 111902.

[16] Wang, K., Zhou, J., Cai, C., Xu, D., and Ouyang, H., 2019. "Mathematical modeling and analysis of a meta-plate for very low-frequency band gap". *Applied Mathematical Modelling,* **73**, pp. 581–597.

[17] Yang, Z., Mei, J., Yang, M., Chan, N., and Sheng, P., 2008. "Membrane-type acoustic metamaterial with negative dynamic mass". *Physical review letters,* **101**(20), p. 204301.

[18] Rupin, M., Lemoult, F., Lerosey, G., and Roux, P., 2014. "Experimental demonstration of ordered and disordered multiresonant metamaterials for lamb waves". *Physical review letters,* **112**(23), p. 234301.

[19] Banerjee, A., Das, R., and Calius, E. P., 2017. "Frequency graded 1d metamaterials: A study on the attenuation bands". *Journal of Applied Physics,* **122**(7), p. 075101.

[20] Liu, C., and Reina, C., 2018. "Broadband locally resonant metamaterials with graded hierarchical architecture". *Journal of Applied Physics,* **123**(9), p. 095108.

[21] Celli, P., Yousefzadeh, B., Daraio, C., and Gonella, S., 2019. "Bandgap widening by disorder in rainbow metamaterials". *Applied Physics Letters,* **114**(9), p. 091903.

[22] Xiao, Y., Mace, B. R., Wen, J., and Wen, X., 2011. "Formation and coupling of band gaps in a locally resonant elastic system comprising a string with attached resonators". *Physics Letters A,* **375**(12), pp. 1485–1491.

[23] Liu, L., and Hussein, M. I., 2012. "Wave motion in periodic flexural beams and characterization of the transition between bragg scattering and local resonance". *Journal of Applied Mechanics,* **79**(1), p. 011003.

[24] Moscatelli, M., Ardito, R., Driemeier, L., and Comi, C., 2019. "Band-gap structure in two-and three-dimensional cellular locally resonant materials". *Journal of Sound and Vibration,* **454**, pp. 73–84.

[25] Hussein, M. I., 2009. "Reduced bloch mode expansion for periodic media band structure calculations". *Proceedings of the Royal Society of London A: Mathematical, Physical and Engineering Sciences,* **465**(2109), pp. 2825–2848.

[26] Fokin, V., Ambati, M., Sun, C., and Zhang, X., 2007. "Method for retrieving effective properties of locally resonant acoustic metamaterials". *Physical review B,* **76**(14), p. 144302.

[27] Nemat-Nasser, S., Willis, J. R., Srivastava, A., and Amirkhizi, A. V., 2011. "Homogenization of periodic elastic composites and locally resonant sonic materials". *Physical Review B,* **83**(10), p. 104103.

[28] Krushynska, A., Kouznetsova, V., and Geers, M., 2014. "Towards optimal design of locally resonant acoustic metamaterials". *Journal of the Mechanics and Physics of Solids,* **71**, pp. 179–196.

[29] Sridhar, A., Kouznetsova, V. G., and Geers, M. G., 2016. "Homogenization of locally resonant acoustic metamaterials towards an emergent enriched continuum". *Computational Mechanics,* **57**(3), pp. 423–435.

[30] Sridhar, A., Kouznetsova, V., and Geers, M., 2017. "A semi-analytical approach towards plane wave analysis of local resonance metamaterials using a multiscale enriched continuum description". *International Journal of Mechanical Sciences,* **133**, pp. 188–198.

[31] Roca, D., Lloberas-Valls, O., Cante, J., and Oliver, J., 2018. "A computational multiscale homogenization framework accounting for inertial effects: application to acoustic metamaterials modelling". *Computer Methods in Applied Mechanics and Engineering,* **330**, pp. 415–446.

[32] Roca, D., Yago, D., Cante, J., Lloberas-Valls, O., and Oliver, J., 2019. "Computational design of locally resonant acoustic metamaterials". *Computer Methods in Applied Mechanics and Engineering,* **345**, pp. 161–182.

[33] McGee, O., Jiang, H., Qian, F., Jia, Z., Wang, L., Meng, H., Chronopoulos, D., Chen, Y., and Zuo, L., 2019. "3d printed architected hollow sphere foams with low-frequency phononic band gaps". *Additive Manufacturing,* **30**, p. 100842.

[34] Claeys, C., Deckers, E., Pluymers, B., and Desmet, W., 2016. "A lightweight vibro-acoustic metamaterial demonstrator: Numerical and experimental investigation". *Mechanical Systems and Signal Processing,* **70**, pp. 853–880.

[35] Leblanc, A., and Lavie, A., 2017. "Three-dimensional-printed membrane-type acoustic metamaterial for low frequency sound attenuation". *The Journal of the Acoustical Society of America,* **141**(6), pp. EL538–EL542.

[36] ASTM E1050-98, 1998. Standard test method for impedance and absorption of acoustical materials using a tube, two microphones, and a digital frequency analysis system. Standard, ASTM International, West Conshohocken, PA.

[37] Xu, Z., Wang, Y., Wu, D., Ananth, K. P., and Bai, J., 2019. "The process and performance comparison of polyamide 12 manufactured by multi jet fusion and selective laser sintering". *Journal of Manufacturing Processes,* **47**, pp. 419–426.

**Figure captions**

Fig. 1. Experiment setup representation of the impedance tubes used for measuring the normal incidence sound transmission loss of a sample LRAM panel. The tube cavity has a 8 cm × 8 cm squared section and each pair of microphones are separated 7.6 cm apart. The frequency range of operation goes from 500 to 2000 Hz. All measures in the figure represent cm. (a) Schematic representation and (b) actual experimental setup.

Fig. 2. Acoustic metamaterial panel design. The panel is stuck to two skins made with the same material, as in the top right corner of the figure, in order to hold and isolate the unit cells. A detailed unit cell design is depicted in the bottom right corner of the figure. Dimensions in millimetres.

Fig. 3. (a) Displacement of the internal vibration mode responsible for the attenuation peak at 1050 Hz and (b) corresponding mode causing the transmission peak indicating the upper bandgap limit at 1380 Hz. The black dashed line indicates the undeformed unit cell contour. Note that in the attenuation peak, the inclusion vibrates keeping the supports fixed (causing the macroscopic wave to effectively stop propagating), while in the transmission peak, the inclusion remains nearly fixed and the supports vibrate (further increasing the wave transmission through the panel).

Fig. 4. Transmission loss simulation set-up. The solid domain consists of two material phases: the standard isotropic 3D-printing material and an internal region where the the actual metamaterial cells can be found. The latter has been modelled as a homogenized material, with the properties obtained from the RVE analysis. Springs of a certain stiffness $k$ have been introduced in the pressed area of both the front and rear faces of the panel, in order to simulate the elastic behaviour of the sealing. In the remaining region, which is the area actually exposed to the acoustic waves inside the tube, an incident, a reflected and a transmitted plane wave have been imposed as depicted in the figure in order to obtain the transmission coefficient.

Fig. 5. Transmission loss results obtained experimentally for the homogeneous sample panels of equivalent mass (blue triangles) and thickness (red crosses) and the metamaterial sample panel (black circles). The results obtained numerically for the metamaterial panel are also given for comparison, both for the undamped case (solid black line) and the case accounting for viscoelastic effects on the material (dashed black line).

**Table headings**
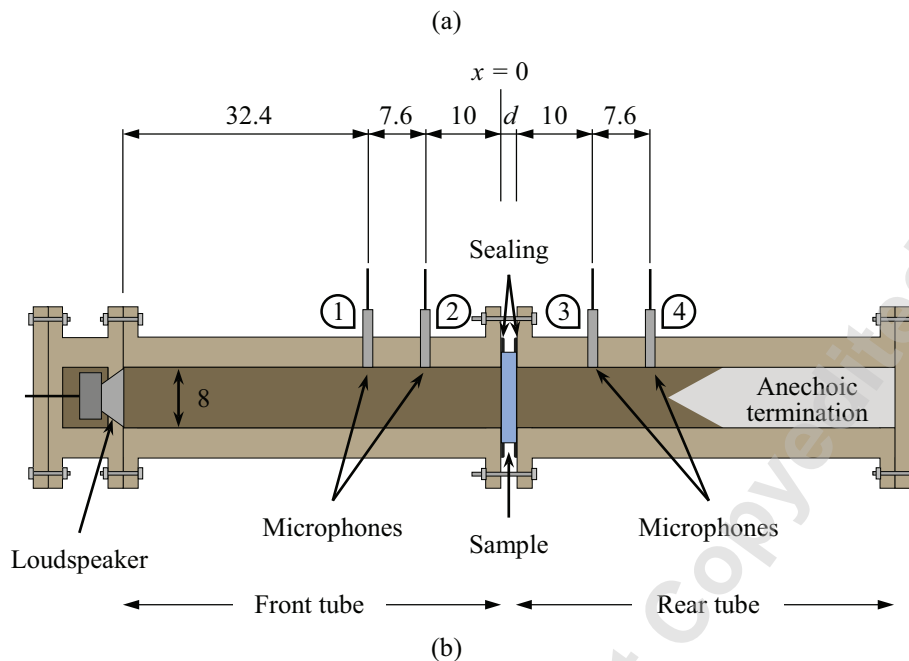
Table 1. 3D-Printing material properties.
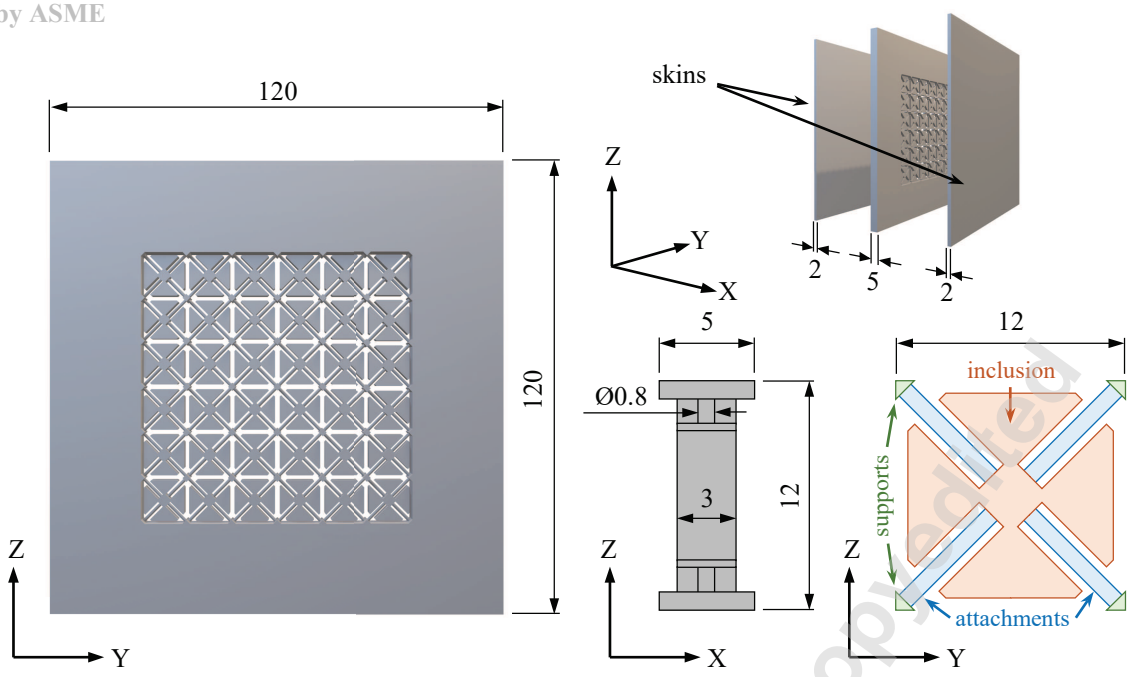
**Figures**

(a)

$x = 0$

32.4    7.6    10    $d$    10    7.6

Sealing

① ② ③ ④

8

Anechoic
termination

Loudspeaker

Microphones    Sample    Microphones

← Front tube →  ← Rear tube →

(b)

Fig. 1.

Fig. 2.
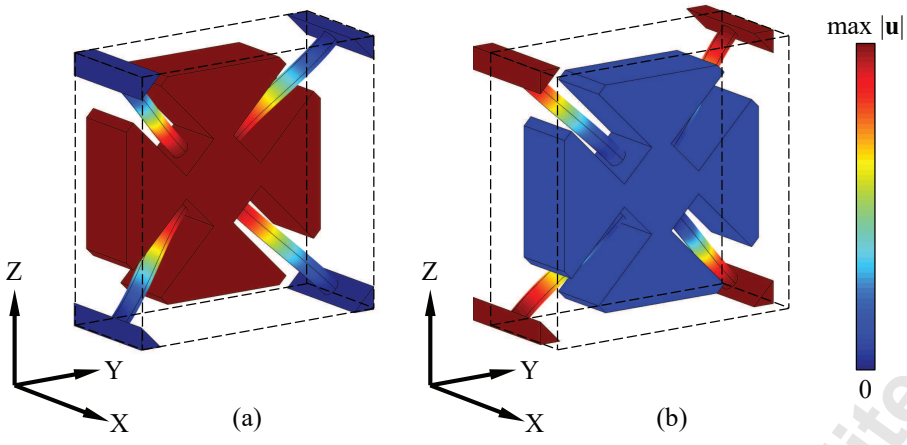
Fig. 3.
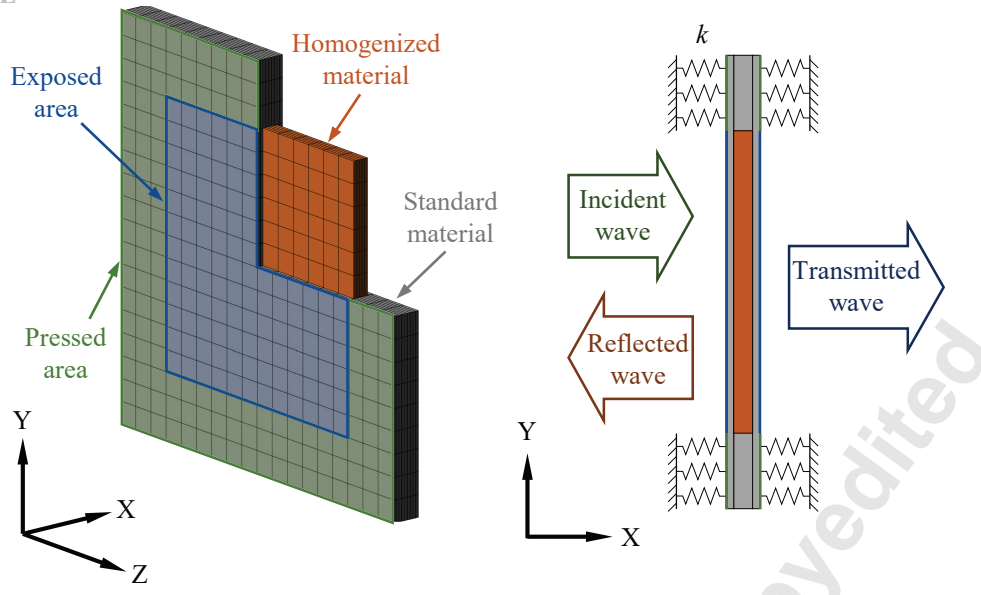
Fig. 4.
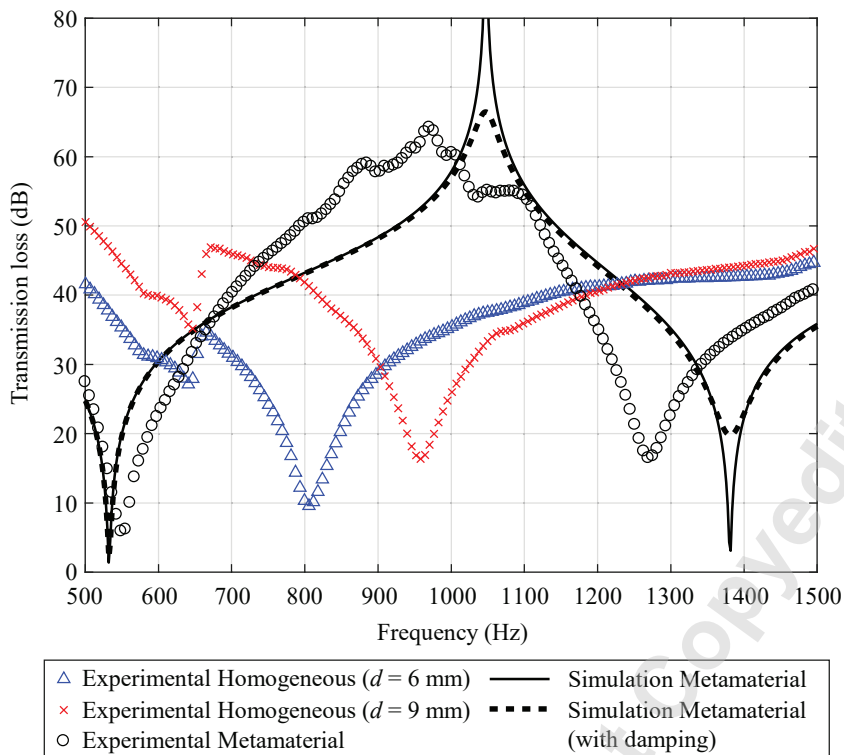
Fig. 5.

**Tables**

Table 1.

| Material | Density (kg/m$^3$) | Young Modulus (MPa) | Poisson ratio |
|----------|--------------------|---------------------|---------------|
| PA 11    | 1050               | 1800                | 0.405         |